

# Measuring collective diffusion properties by counting particles in boxes

Adam Carter,<sup>1</sup> Eleanor K. R. Mackay,<sup>2</sup> Brennan Sprinkle,<sup>3</sup> Alice L. Thorneywork,<sup>2</sup> and Sophie Marbach<sup>4,\*</sup>

<sup>1</sup>*Sorbonne Université, Physicochimie des Electrolytes et Nanosystèmes Interfaciaux, F-75005 Paris, France*

<sup>2</sup>*Physical and Theoretical Chemistry Laboratory, South Parks Rd, Oxford, OX1 3QZ UK*

<sup>3</sup>*Applied Math and Statistics, Colorado School of Mines, 1500 Illinois St, Golden, CO 80401*

<sup>4</sup>*CNRS, Sorbonne Université, Physicochimie des Electrolytes et Nanosystèmes Interfaciaux, F-75005 Paris, France*

(Dated: December 19, 2024)

Collective diffusion, characterised by the collective diffusion coefficient  $D_{\text{coll}}$ , is a key quantity for describing the macroscopic transport properties of soft matter systems. However, measuring  $D_{\text{coll}}$  is a fundamental experimental and numerical challenge, as it either relies on nonequilibrium techniques that are hard to interpret or on Fourier-based approaches at equilibrium which are fraught with difficulties associated with Fourier transforms. In this work, we present a novel approach to measure collective diffusion properties by analysing the statistics of particle number counts  $N(t)$  in virtual observation boxes of an image at equilibrium, a method we term the ‘‘Countscope’’. By investigating the equilibrium diffusive dynamics of a 2D colloidal suspension experimentally and numerically, we demonstrate this method can accurately measure  $D_{\text{coll}}$ . We validate our results against Fourier-based approaches and establish best practices for measuring  $D_{\text{coll}}$  using fluctuating counts. Remarkably, Fourier techniques struggle with long-range collective measurements because of the non-periodic nature of an experimental image, yet counting fully exploits this property by deliberately using finite observation windows. Finally, we discuss the potential of our method to advance our understanding of collective properties in suspensions, particularly the role of hydrodynamic interactions.

Understanding the motion of an ensemble of particles, or collective motion, is a fundamental puzzle in soft matter, from determining how molecules traverse a porous matrix [1–3] to learning how interactions between active or living particles trigger spontaneous group motion [4–7]. A canonical example of collective motion is collective diffusion [8]. Following the seminal works of Stokes and Einstein [9], we understand the diffusion of a single particle suspended in a fluid as resulting from the action of thermal motion of fluid molecules on the particle. This diffusion is characterised through the slope of the particle’s mean-squared displacement, which provides the *bulk* or *free* diffusion coefficient  $D_0 = k_B T / \gamma$ , where  $k_B T$  is the unit of energy and  $\gamma$  a friction coefficient (Fig. 1-a). When a particle diffuses in a suspension of particles, its *self* diffusion coefficient  $D_{\text{self}}$  may differ from  $D_0$  due to interparticle interactions (Fig. 1-b). In contrast, when a density gradient forms in a particle suspension, the so-called *collective* diffusion coefficient  $D_{\text{coll}}$  characterises the relaxation of the gradient, which is inherently a many particle behaviour (Fig. 1-c). Note that this coefficient is sometimes referred to as the transport diffusion coefficient, and we refer the reader to Ref. [10] for an overview.

Collective diffusion is useful to characterize the macroscopic transport properties of a system. For example, in a suspension with repulsive interactions, self-diffusion is hindered by neighbouring particles inducing spatial constriction, while collective diffusion is enhanced as moving particles push their neighbours, facilitating relaxation. This yields  $D_{\text{self}} \leq D_0 \leq D_{\text{coll}}$ . A theoretical

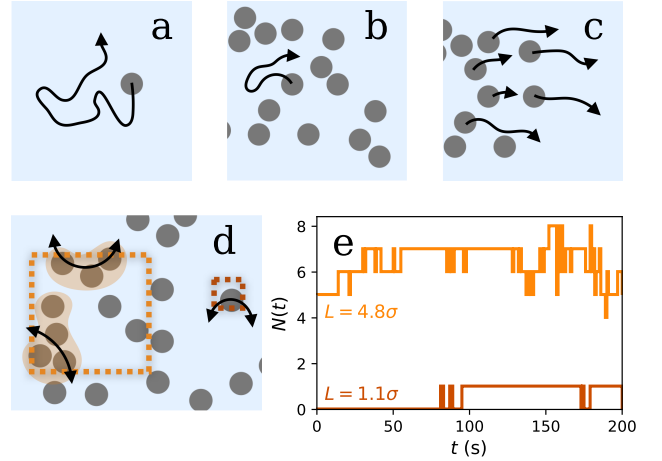


**FIG. 1. Inferring collective diffusion properties from counts.** Diffusion properties can refer to (a) the bulk or free diffusion coefficient of a particle  $D_0$  suspended in a fluid, (b) the self-diffusion of a particle  $D_{\text{self}}$  in a suspension or (c) the collective diffusion coefficient of the suspension  $D_{\text{coll}}$ , that describes the relaxation of a particle density gradient. (d) Here, we show how to measure  $D_{\text{coll}}$  from the relaxation of groups of particles at equilibrium in large virtual observation boxes on an image (orange). Counts in small boxes (red) probe individual motion. (e) The number of particles  $N(t)$  in a box fluctuates due to individuals or groups of particles diffusing in and out of the box.

argument considering only pair-wise interactions shows  $D_{\text{coll}} = D_0 / S(k = 0)$ , where  $S(k = 0)$  is the structure factor of the suspension at vanishing wavevector [8, 11]. At high particle densities in colloidal suspensions,  $S(k = 0)$  can be substantially smaller than 1, and  $D_{\text{coll}}$

\* sophie.marbach@cnrs.fr

may be significantly larger than  $D_0$ . In addition to direct interactions set by the interparticle potential, the suspending fluid also introduces hydrodynamic interactions. However, even for suspensions of hard sphere-like colloids, experimental results widely differ in assessing the role of hydrodynamic interactions on collective properties [12–22].

Such discrepancies arise from the challenge of measuring collective diffusion coefficients, both experimentally and numerically. Since collective diffusion manifests out-of-equilibrium, several investigations explore the relaxation of a number density gradient [23–26]. However, such experiments are hard to repeat, because they require setting up the system out-of-equilibrium at the beginning of each experiment. In addition, as the density gradient relaxes, neither the gradient nor the local density is constant, which makes it hard to disentangle how  $D_{\text{coll}}$  depends on particle number density. Collective diffusion can also be probed in equilibrium, from density fluctuations that occur due to thermal motion. The relaxation of the density fluctuations is then investigated through the so-called dynamic structure factor calculated in Fourier space [8]. Yet, Fourier transforms are computationally demanding and fraught with spurious features due to edge effects on microscopy images [27–29].

We propose to use a novel approach to measure collective diffusion properties experimentally and numerically by investigating the statistics of particle number counts  $N(t)$  in virtual observation boxes at equilibrium (Fig. 1-d). The number  $N(t)$  fluctuates due to particles diffusively entering and exiting a box (Fig. 1-e). For small observation boxes, fluctuations are dominated by individual particle motion. Large observation boxes sense collective motion since fluctuations occur due to the motion of groups of particles. This idea, termed the “Countscope”, was proposed recently by some of us to probe self diffusion, yet its potential to probe collective diffusion is not conclusively explored [22]. For example, among collective properties, are fluctuating counts indeed sensitive to  $D_{\text{coll}}$ ? Can we build a workflow and understand best practices to extract  $D_{\text{coll}}$  from experimental data? And how do fluctuating counts compare with existing methods to measure collective properties?

In this work, we investigate the equilibrium diffusive dynamics of 2D colloidal suspensions experimentally and numerically with fluctuating counts (Sec. I). We demonstrate that counting is indeed sensitive to  $D_{\text{coll}}$  in the limit of large box sizes. Beyond  $D_{\text{coll}}$ , counting can illuminate the relaxation dynamics at all lengthscales via a box-size dependent diffusion coefficient  $D(L)$  where  $L$  is the size of the square box. We establish a robust double-workflow to measure  $D_{\text{coll}}$  and  $D(L)$ : either via a simple fit of the data (Sec. II B), or obtaining the relaxation timescale of fluctuations via data integration (Sec. II C). We determine best analysis practices and discuss perspectives to optimize this measurement. We

compare our results with Fourier approaches based on investigations of the dynamic structure factor and discuss the limitations of counting and Fourier techniques (Sec. III). Fourier techniques are intrinsically limited by the finite field of view, as images are non-periodic. Remarkably, counting exploits this intrinsic experimental feature by paving the space with finite virtual observation boxes. Finally, we discuss how our methodology could provide further insights into the collective properties of suspensions, particularly in understanding the role of hydrodynamic interactions (Sec. IV).

## I. BRIEF INTRODUCTION TO THE COUNTSCOPE WITH OVERLAPPED BOXES

*a. 2D colloidal suspension near a wall.* We investigate the collective diffusive relaxation of a 2D suspension of colloids experimentally and numerically. We briefly recapitulate the system’s properties here and refer to Ref. [22] for details.

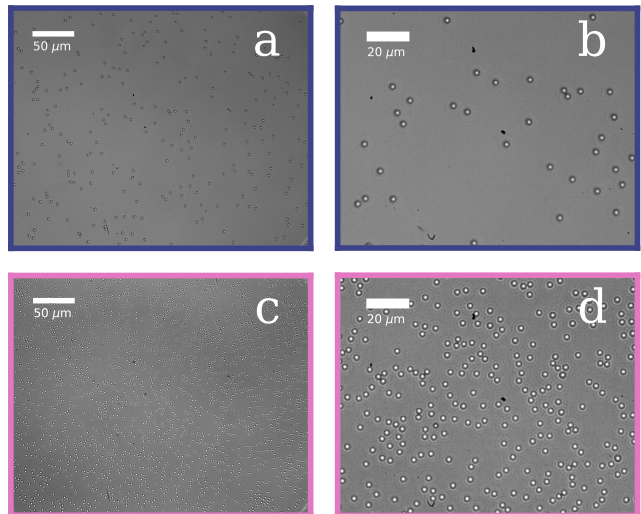


FIG. 2. **2D experimental hard-sphere system.** Optical images of (a,b, dark blue) the dilute  $\phi = 0.02$  and (c,d, pink) the dense  $\phi = 0.11$  suspensions. (a,c) shows the entire field of view and (b,d) a cropped subset for visualization.

In experiments, particles, with effective hard sphere diameter  $\sigma = 3.0 \mu\text{m}$ , are gravitationally confined to the base of a glass cell and represent well a hard sphere model [30, 31]. Suspensions are imaged using a custom-built inverted microscope with particle positions acquired from images using standard particle tracking protocols [32, 33]. For simplicity, we explore here only two different packing fractions, corresponding to a dilute ( $\phi = 0.02$ ) and dense ( $\phi = 0.11$ ) suspension – see Fig. 2. Note that while  $\phi = 0.11$  lies far below the crystallisation transition for these systems, this packing fraction is sufficiently dense that interactions play a significant role. Importantly, however, these interactions

do not result in such long timescales that the full dynamic properties are not accessible over reasonable experimental timescales. To obtain statistically accurate data over the long collective relaxation timescales we investigate, we acquire experimental data over 20 h. The optical stage and experimental conditions were carefully adjusted to avoid any significant drift over that long timescale.

In parallel, we conduct Brownian dynamics simulations representative of the experimental system, including hydrodynamic lubrication with the bottom glass wall [34]. Simulation parameters are all set to their experimentally measured values, and steric forces are modelled using the hard potential in Eq. (31) of Ref. [34]. Hydrodynamic lubrication between particles is not accounted for, and is not necessarily expected to play a significant role at the two studied packing fractions. Further numerical and simulation methods are described in Appendix A.

*b. Number fluctuations in observation boxes.*

For both experiments and simulations, we sample fluctuations of the number of particles  $N(t)$  within square boxes of size  $L \times L$  over time.  $N(t)$  fluctuates between discrete values as a consequence of particles moving in and out of the box via diffusion (Fig. 1-e). We explore the statistical properties of this random number  $N(t)$ . We can compute the correlation function depending on the lag time  $t$  as

$$C_N(t) = \langle N(t+t_0)N(t_0) \rangle - \langle N \rangle^2 \quad (1)$$

where  $\langle \cdot \rangle$  indicates an average over all boxes and time origins  $t_0$  within the acquisition. For simplicity, in the following, we write  $t_0 = 0$ . Notice that when the lag time vanishes,  $C_N(0) = \langle N^2 \rangle - \langle N \rangle^2 \equiv \text{Var}(N)$ . Another relevant quantity is the mean squared change in particle number,

$$\begin{aligned} \langle \Delta N^2(t) \rangle &= \langle (N(t) - N(0))^2 \rangle \\ &= 2(\langle N^2 \rangle - \langle N \rangle^2) - 2(\langle N(t)N(0) \rangle - \langle N \rangle^2) \\ &= 2\text{Var}(N) - 2C_N(t). \end{aligned} \quad (2)$$

Both statistical quantities will be useful to investigate as they characterize the dynamical relaxation of number fluctuations. In Fig. 3-a, we plot the mean squared change in particle number,  $\langle \Delta N^2(t) \rangle$ , for different box sizes in the dilute regime ( $\phi = 0.02$ ).  $\langle \Delta N^2(t) \rangle$  first increases in time. Starting from an initial condition with  $N(0)$  particles in a box, as time goes by, one is more and more likely to see configurations where  $N(t)$  is much higher or much smaller than  $N(0)$ , resulting in an overall increase of the squared difference  $(N(t) - N(0))^2$  on average. Eventually, there is a complete exchange between particles inside the box with those outside and we observe a plateau. The number of particles at long times is therefore uncorrelated with that in the initial configuration, *i.e.*  $C_N(t) \simeq 0$  for long times (Fig. 3-b).

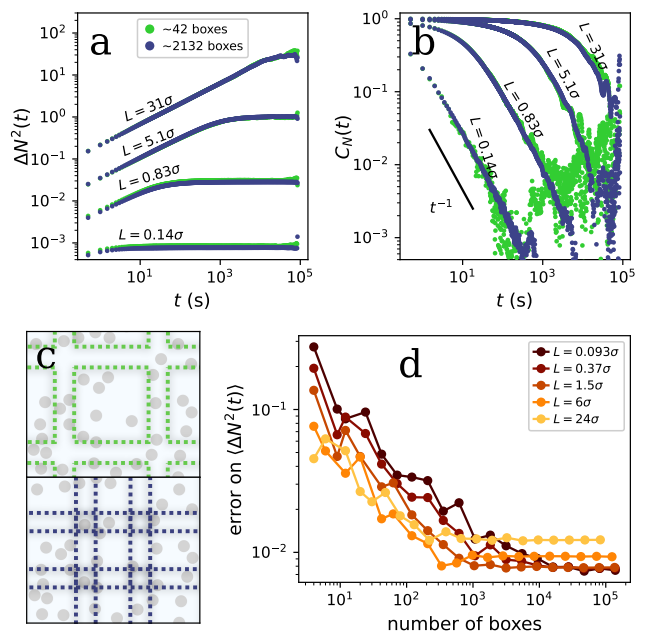


**FIG. 3. Importance of overlapping observation boxes.** (a) Number fluctuations  $\langle \Delta N^2(t) \rangle$  and (b) correlation function  $C_N(t)$  as a function of the lag time  $t$  for several box sizes for the dilute suspension  $\phi = 0.02$ . Experimental data. Legend is shared between a and b. (c) Schematic illustrating box overlapping. (d) Normalised average standard error on  $\langle \Delta N^2(t) \rangle$  with respect to the number of observation boxes for different box sizes. The error is calculated by dividing the experimental data at  $\phi = 0.02$  into 10 chunks in time, computing  $\langle \Delta N^2(t) \rangle$  for each chunk, and finding the (averaged over time) standard error between chunks.

From Eq. (2), the plateau corresponds to the variance  $\langle \Delta N(t \rightarrow \infty) \rangle = 2\text{Var}(N)$ .

In Ref. [22], we established that number fluctuations can resolve the self-diffusion coefficient of particles  $D_{\text{self}}$ . Indeed, at short times, fluctuations are dominated by individual particles entering or exiting boxes and number fluctuations satisfy  $\langle \Delta N^2(t) \rangle \sim \sqrt{D_{\text{self}} t / L^2}$ . In a system with no interactions, the fluctuations relax over a timescale of about  $L^2 / D_{\text{self}}$ . Yet for dense suspensions, over longer timescales, and especially in large boxes, the motion of groups of particles, or collective dynamics, should affect number fluctuations.

*c. Overlapping boxes.* In this work, we aim to characterise the relaxation of number fluctuations, especially at large length scales – in large boxes – where collective dynamics are at play. Obtaining statistically accurate data over large boxes can be optimized by carefully choosing how to distribute boxes spatially. With separated boxes (Fig. 3-c, green case), as in Ref. [22], statistical information is greatly reduced at large scales, with significant unused regions on an image. Instead, we propose to overlap sampling boxes (Fig. 3-c, blue case), significantly increasing the number of

observation boxes. Qualitatively, overlapping boxes improve the resolution of the plateau of  $\langle \Delta N^2(t) \rangle$  (Fig. 3-a), and significantly reduce noise on the long tails of the correlation function  $C_N(t)$  (Fig. 3-b). This means that, although one obtains somewhat correlated data with overlapped boxes, the amount of information is more important and improves statistical resolution.

To understand what degree of overlapped boxes yields best statistics, we evaluate the average standard error on  $\langle \Delta N^2(t) \rangle$  as we increase the number of boxes, and hence the amount of overlap between boxes (Fig. 3-d). The error decreases by an order of magnitude with increasing box numbers, confirming overlapped boxes significantly improve statistical accuracy. Eventually the error reaches a noise floor: as we pave space with boxes, boxes eventually become so overlapped that they are redundant and no more information to be gained. Since this excessive overlap clearly happens with fewer boxes for larger boxes, the noise floor is reached with fewer boxes for large boxes than small ones. Overall, this suggests an upper limit for the number of boxes to use, which we take here to be 2000 boxes for our system parameters. We use this overlapping technique and bound in all future analysis.

## II. COUNTOSCOPE TO MEASURE COLLECTIVE DIFFUSION PROPERTIES

We now investigate methods to extract relaxation of number fluctuations, especially in large boxes, and see how they relate to collective diffusion properties. The two statistical quantities,  $\langle \Delta N^2(t) \rangle$  and  $C_N(t)$ , allow us to explore two complementary methods based on the Countoscope, to extract collective dynamics. Method 1 (Sec. II-B), obtains a box-size dependent diffusion coefficient  $D(L)$  via a phenomenological fit of the number fluctuations  $\langle \Delta N^2(t) \rangle$ . Method 2 (Sec. II-C) infers a relaxation timescale  $T(L)$  by integrating the correlation function  $C_N(t)$ , relating to  $D(L)$  as  $T(L) \propto L^2/D(L)$ . We will compare results between an effectively non-interacting case, the dilute suspension at  $\phi = 0.02$ , and the dense suspension at  $\phi = 0.11$  where interactions modify behaviour. We will also explore differences between experimental data, simulations and theory. Importantly, we will show  $D(L)$  interpolates between two regimes, a regime in which self-diffusion dominates in small boxes (red in Fig. 1-d) and collective diffusion in large boxes (orange in Fig. 1-d). We start by highlighting these different regimes, and then establish Methods 1 and 2.

### A. Two regimes of box sizes: small for individual dynamics and large for collective.

*a. Theory highlights two limit regimes of box sizes.* To understand how to probe a meaningful quantity from

number fluctuations, we first examine the behaviour of  $\langle \Delta N^2(t) \rangle$  in the light of theory. Predictions for such correlation functions can be obtained using stochastic density field theory (Dean-Kawasaki equations) [35, 36]. In the absence of interparticle interactions, some of us have shown ([22, 37]) that  $\langle \Delta N^2(t) \rangle$  obeys the analytical law

$$\langle \Delta N^2(t) \rangle = 2\langle N \rangle \left( 1 - \left[ f \left( \frac{4D_{\text{self}}t}{L^2} \right) \right]^2 \right), \quad (3)$$

where  $f$  has the explicit expression

$$f \left( \tau = \frac{4D_{\text{self}}t}{L^2} \right) = \sqrt{\frac{\tau}{\pi}} \left( e^{-1/\tau} - 1 \right) + \text{erf} \left( \sqrt{1/\tau} \right) \quad (4)$$

and in the absence of interactions we recall  $D_{\text{self}} = D_0$ . Eq. (3) perfectly agrees with experimental data in the dilute regime (see SI Fig. S1). Eq. (3) can be modified to account for steric repulsion between particles, leading to a slightly more complicated expression for  $\langle \Delta N^2(t) \rangle$  [22], that we recall in Eq. (12) in Appendix B. This modified expression is hard to use directly, as it involves the suspension's structure factor  $S(k)$  for a given wavelength  $k$ . Yet, one can recover simple expressions in the limit of small and large box sizes (Appendix B). In the limit of small boxes  $L \ll \sigma$ , number fluctuations are described by Eq. (3): even in a dense suspension, a small box probes the motion of an individual particle. In the limit of large boxes,  $L \gg \sigma$ , remarkably one finds

$$\langle \Delta N^2(t) \rangle \simeq 2 \text{Var}(N) \left( 1 - \left[ f \left( \frac{4D_{\text{coll}}t}{L^2} \right) \right]^2 \right) \quad (5)$$

where  $D_{\text{coll}} = D_{\text{self}}/S(k=0)$ . Notice the similarity of Eq. (5) to Eq. (3). The prefactor  $\langle N \rangle$  in Eq. (3) is replaced by the variance of the number of particles in a box  $\text{Var}(N)$ . For these large boxes, we note that  $\text{Var}(N) = S(k=0)\langle N \rangle$ , a well-established link in liquid matter [11, 22, 38]. Instead of  $D_{\text{self}}$  in Eq. (3), the relevant diffusion constant is now  $D_{\text{coll}}$ . At these large lengthscales, collective effects dominate, as the relaxation of number fluctuations is governed by groups of particles going in and out of a box, see the orange highlighted groups in the schematic of Fig. 1-d. The collective diffusion coefficient  $D_{\text{coll}}$  characterizes dynamics, hinting that the Countoscope could indeed be sensitive to  $D_{\text{coll}}$ .

*b. Individual and collective regimes are fully apparent in simulations and experiments.* To confirm the presence of these limiting regimes, we plot  $\langle \Delta N^2(t) \rangle$  in the dense system, rescaling time by  $L^2$  and  $\langle \Delta N^2(t) \rangle$  also by  $L^2$ , for simulations and experiments (Fig. 4-a and b). On each plot, we also present the limiting regimes Eq. (3) (dotted) and Eq. (5) (dashed). In the simulations, small and large box data indeed converge to the limiting regimes. In the experiments, the agreement with the collective regime is less clear. This is in part due to fewer statistics on the experimental data; but could

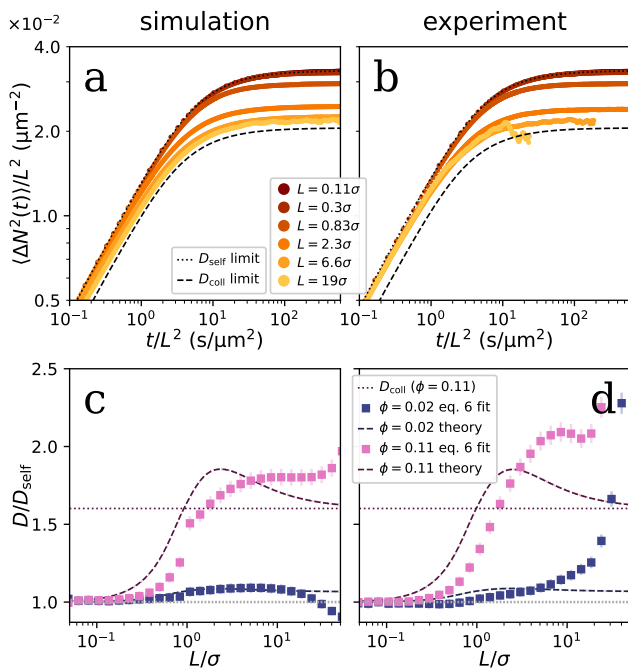


FIG. 4. **Method 1: phenomenological fitting of number fluctuations.** (a-b) Rescaled  $\langle \Delta N^2(t) \rangle$  versus rescaled time for (a) simulations and (b) experimental data in the dense  $\phi = 0.11$  regime. Box sizes go from small (dark red) to large (yellow). Dashed curves represent the limit regimes Eq. (3) and Eq. (5). (c-d) Obtained  $D(L)$  from  $\langle \Delta N^2(t) \rangle$  fits of Eq. (6) for (c) simulations and (d) experimental data. Lines correspond to the theory Eq. (8). Blue corresponds to the dilute regime, and pink the dense.

also be due to collective hydrodynamic effects, that are not accounted for in the theory or in the simulations in Fig. 4-a. Nonetheless, curves converge to a limit regime at large length scales.

## B. Method 1: phenomenological fit of number fluctuations

*a. Workflow of method 1.* To investigate the box-size dependent relaxation speed, we thus seek a box-size dependent diffusion coefficient  $D(L)$ . Considering the similarity between Eq. (3) and Eq. (5), we introduce the *phenomenological fitting law* for any box size as

$$\langle \Delta N^2(t) \rangle = 2 \text{Var}(N) \left( 1 - \left[ f \left( \frac{4D(L)t}{L^2} \right) \right]^2 \right) \quad (6)$$

where  $D(L)$  is a fitting parameter at every box size. Note that since  $\text{Var}(N) = \langle N \rangle$  for small boxes (Fig. S1), then Eq. (6) indeed describes number fluctuations of small boxes provided  $D(L \ll \sigma) = D_{\text{self}}$ . Eq. (6) also converges to the large box regime, provided  $D(L \gg \sigma) = D_{\text{coll}}$ .

*b. Scale-dependent diffusion coefficient  $D(L)$  from method 1.* Based on this phenomenological fitting law, one can obtain predictions for the scale-dependent diffusion coefficient  $D(L)$  as shown in Fig. 4-c and d, again for simulations and experiments. For reference, we also add theory curves for  $D(L)$ , which we will comment on further in method 2. At this stage, it is sufficient to know theory curves converge to  $D_{\text{coll}}$  for  $L \gg \sigma$ , and we use mostly this limit as a reference. For the dense regime  $\phi = 0.11$ , the theory predicts  $D_{\text{coll}} = D_{\text{self}}/S(k=0) \simeq 1.6D_{\text{self}}$  (dotted lines in Fig. 4-c and d).

In the dense regime  $\phi = 0.11$ ,  $D(L)$ , for simulations and experiments, interpolates between 2 limiting cases:  $D(L)$  plateaus for small boxes, and then increases before reaching another larger plateau. For small boxes  $L \ll \sigma$ , we find  $D(L) \simeq D_{\text{self}}$ , the box-dependent diffusion coefficient probes individual motion, as expected. In contrast, in larger boxes, group motion dominates and increases the effective diffusion coefficient  $D(L)$ . The hard sphere repulsion between particles accelerates group diffusion: a single particle's motion can influence that of its neighbours via repulsion, and of the subsequent neighbours.

The plateau reached in large boxes for experimental data is much larger than the expected  $D_{\text{coll}}$ . This could be associated with collective hydrodynamic interactions not accounted for in the predicted  $D_{\text{coll}}$ . Yet, in the simulations, which do not include hydrodynamic interactions, the plateau reached is also slightly higher than the predicted  $D_{\text{coll}}$ . This is likely an artefact of the phenomenological fitting. At short enough times, the number fluctuations are dominated by individual particles entering and exiting a box – curves all agree with Eq. (3) (Fig. 4, dotted black line). The phenomenological fit uses a single diffusion coefficient to model both this early-time individual behaviour and long-time collective, resulting in a slightly larger  $D(L)$  for large boxes than  $D_{\text{coll}}$ . The phenomenological fit could thus be improved by fitting long-time evolution only, but for simplicity, we do not investigate this here. The phenomenological fit Eq. (6) thus only provides qualitative insights into the emergence of collective phenomena at large scales.

Compared to the dense case  $\phi = 0.11$ , the variations in  $D(L)$  are less apparent in the dilute regime,  $\phi = 0.02$ , which is expected as collective effects should not significantly modify dynamics at this low packing fraction. Nonetheless, a slight increase of  $D(L)$  is still observed, showing the sensitivity of the technique even to mild differences in collective versus individual properties.

*c. Best practices for obtaining the phenomenological fit - difficulty of resolving variances accurately.* In both experiment and simulation data, at both packing fractions, we observe divergences in the computation at large scales  $L \gtrsim 20\sigma$ . These are due to statistical accuracy, which we comment on now. The phenomenological fit Eq. (6) relies on an estimate of the variance  $\text{Var}(N)$ . Accurate determination of the variance

is challenging, especially for large boxes. In fact, our 2D system requires long times to sample many different states. A long-time scaling law can be obtained from the theory Eq. (3) and shows  $C_N(t)$  decorrelates extremely slowly, as  $1/t$  (see Fig. 3-b). This is a consequence of the fact that diffusing particles can always return to their starting point in 2D [39]. In a nutshell, resolving  $\text{Var}(N)$  in 2D requires significantly long datasets.

In experiments, for boxes  $L \gtrsim 20\sigma$ , it becomes apparent that  $\text{Var}(N)$ , equivalently the plateau in  $\langle \Delta N^2(t) \rangle$ , becomes increasingly hard to resolve. In Fig. 4-b, on the largest yellow box,  $L \simeq 20\sigma$ , we see significant noise near the plateau region. Due to the slow decay of number correlations, we expect experiments need to be at least as long as the decorrelation time to resolve  $\text{Var}(N)$  correctly. Indeed, for  $L = 20\sigma$ , the decorrelation time is at most  $T \simeq L^2/D_0 \simeq 23$  h. Since this is about the duration of our experiments, this justifies that divergences appear in Fig. 4-d for  $L \gtrsim 20\sigma$ . Generally, this defines an upper box size that can be resolved in an experiment, as  $L \lesssim \sqrt{D_0 T_{\text{exp}}}$  where  $T_{\text{exp}}$  is the experiment time.

Simulations can be conducted for long enough times that, in principle, decorrelation should not be such an issue. Yet, we find reliable variance estimates are also hard to access for large boxes  $L \gtrsim 0.3L_x$  where  $L_x$  is the size of the periodic simulation box (see SI fig S4). Indeed, collective dynamics loop back onto themselves via the periodic boundary conditions, and hence large simulation boxes are needed for accurate resolution. This thus defines an upper box size that can be resolved in a simulation, as  $L \simeq 0.3L_x$ . Here we have  $L_x = 640 \mu\text{m}$  and so  $L \lesssim 60\sigma$ .

In this work, we take the variance as an average over all boxes and all times. To estimate the variance from such time-correlated data, other strategies such as bootstrapping could be used [40]. Here, we instead tested different fitting schemes, for instance leaving the variance's value as a free parameter in the phenomenological fitting law Eq. (6). We find an independent estimate of the variance yields the most stable results, and we review further fitting options in SI Fig. S3. Improved fitting strategies could also focus on fitting only to long time scales  $t \geq \sigma^2/D_0$  for large enough boxes. Finally, to avoid overfitting specific timescales, we take logarithmically spaced time points for the least-squares fit.

### C. Method 2: Decorrelation timescale of number fluctuations

While method 1 provides physical intuition on the collective dynamics, it relies on a phenomenological model, Eq. (6), for interpretation. We now expose another method to extract scale-dependent diffusion coefficients exactly. An important advantage is that method 2 can also be performed at large enough length

scales without the knowledge of a model *a priori*.

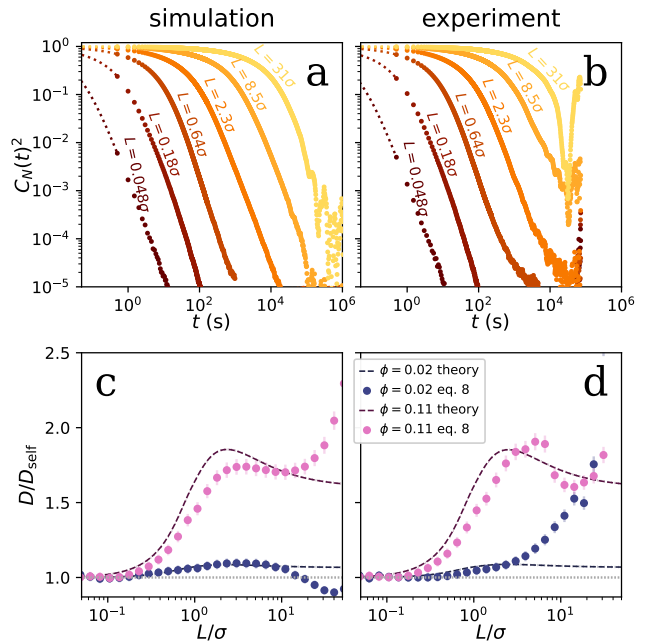


FIG. 5. **Method 2: Decorrelation timescale of number fluctuations.** (a-b) Correlation functions  $C_N(t)^2$  versus time for (a) simulations and (b) experimental data in the dense  $\phi = 0.11$  case. Box sizes go from small (dark red) to large (yellow). Dotted curves for  $t \leq 0.5$  s represent short-time extensions to improve the accuracy of the integral of  $C_N(t)^2$  on small boxes  $L \leq \sigma$ . (c-d) Diffusion coefficient  $D(L) \propto L^2/T(L)$ , where  $T(L)$  is obtained from the integral of  $C_N(t)^2$  from (a-b) for (c) simulations and (d) experimental data. Dashed lines correspond to the theory Eq. (7) (using also Eq. (12)). Blue corresponds to the dilute, and pink the dense regime.

*a. Workflow of method 2.* Method 2 is based on quantifying the relaxation time of the correlation function  $C_N(t)$  (see Fig. 5-a and b). As particles diffusively enter and exit the box, the correlation function decays until it fully decorrelates at long times as particles have completely exchanged between inside and outside the box. To quantify the timescale  $T(L)$  of this decay, Ref. [22] suggested to integrate  $C_N(t)$  as

$$\begin{aligned} T(L) &= 2 \int_0^\infty \left( \frac{C_N(t)}{C_N(0)} \right)^2 dt \\ &= 2 \int_0^\infty \left( 1 - \frac{1}{2} \frac{\langle \Delta N^2(t) \rangle}{\text{Var}(N)} \right)^2 dt. \end{aligned} \quad (7)$$

This definition means that for correlations that decay exponentially,  $T$  would represent the timescale of the decay as  $C_N(t)/C_N(0) = \exp(-t/T)$ . Note, here the unusual squaring factor in the integrand ensures that the integral converges, as the correlation function decays algebraically at long times,  $C_N(t \rightarrow \infty) \sim 1/t$  [22, 39] (Fig. 3-b). Visually,  $T(L)$  also roughly corresponds to the corner in the  $\langle \Delta N^2(t) \rangle$  curves. Considering we have

obtained predictions for  $C_N(t)$  (see Eq. (12) in Appendix B),  $T(L)$  can also be calculated analytically.

In the dilute regime, one can verify analytically and experimentally that  $T$  corresponds to the time to diffuse across the box,  $T(L) = \alpha_T L^2 / 4D_0$  where  $\alpha_T \simeq 0.56$  is a numerical constant whose lengthy expression is reported in Eq. (22). For dilute or non-interacting systems, rescaling time by  $L^2$  is sufficient to describe the relaxation of fluctuations at all scales (see SI fig S1). At higher packing fractions, a simple rescaling of the data fails (see Fig. 4-a and b), indicating that the time required to relax fluctuations does not solely depend on how long a single particle takes to diffuse over the length scale  $L$ . Instead, it should depend on the motion of multiple interacting particles.

We can relate  $T$  to a diffusive phenomenon, by defining a diffusion coefficient dependent on the box size, as

$$D(L) = \alpha_T \frac{L^2}{4T(L)}. \quad (8)$$

With this definition, one can check indeed that  $D(L \ll \sigma) = D_{\text{self}}$  and  $D(L \gg \sigma) = D_{\text{coll}} = D_{\text{self}}/S(k=0)$ . We present  $D(L)$  in Fig. 5-c and d for simulations and experiments (dots) and theory (dashed lines). To facilitate comparison, the same theory was reported in Fig. 5-c and d.

*b. Scale-dependent diffusion coefficient  $D(L)$  from method 2.* Similarly as in Fig. 4, for the dense  $\phi = 0.11$  case (pink), both for simulations and experiments,  $D(L)$  plateaus for small boxes, increases, and then appears to plateau again before hitting a divergent region – the latter of which we comment on in paragraph *c*, and which is also due to limited statistical accuracy. For small boxes  $L \lesssim \sigma$ , we find  $D(L) \simeq D_{\text{self}}$ , the box-dependent diffusion coefficient probes individual motion, as expected. Group motion then increases the effective diffusion coefficient  $D(L)$ .

In the simulations (Fig. 5-c),  $D(L)$  reaches a plateau, around  $L \simeq 10\sigma$ , which corresponds closely with the expected value of the collective diffusion coefficient  $D_{\text{coll}}$  of the suspension. Over nearly the full range of box sizes,  $D(L)$  from method 2 is in good agreement with the theory predictions. This demonstrates the ability of the timescale integral to capture the details of the collective relaxation process. In addition, it confirms that method 2 indeed probes  $D_{\text{coll}}$  for large boxes.

Agreement between theory and experimental data from method 2 (Fig. 5-d) is equally satisfying within the range of boxes where high resolution can be achieved. Whether the discrepancy between experiments, simulations and theory can be attributed to hydrodynamic interactions is still an open question, as the lengthscales involved become too large for accurate resolution.

Finally, experiments, simulations and theory highlight the presence of a peculiar maximum in the  $D(L)$  curves, near  $L \simeq 3 - 5\sigma$  in the dense case  $\phi = 0.11$ . This

effect is quite subtle, and here we propose a qualitative explanation. For small box sizes,  $L \ll \sigma$ , one probes individual motion at small lengthscales, corresponding to a timescale much smaller than the mean time between collisions. For large box sizes,  $L \gg \sigma$ , one probes collective motion (motion of groups) at scales much larger than these transient particle groups, in essence at a mean-field level. For intermediate yet small box sizes, say  $L \simeq \sigma$ , one still probes individual motion but at a scale where a particle senses its neighbours. The interacting neighbours facilitate relaxation of number fluctuations, by pushing one another. This results in an increase of effective dynamics  $D(L)$ . This increased  $D(L)$  can exceed  $D_{\text{coll}}$ , coarsely speaking, because the box is still small enough,  $L \simeq \sigma$ , that the magnitude of the number fluctuations that relax is still small on average. Schematically speaking, at these scales one still investigates only individual particles that get effectively pushed out by their neighbours, resulting in a maximum of  $D(L)$ . We will comment on such interactions further in Ref. [39].

*c. Best practices for obtaining the timescale integral.* We now comment on the divergences observed for  $L \gtrsim 20\sigma$  on experimental and simulation data of  $D(L)$ . To perform the integral in Eq. (7), one must obtain an accurate estimate of the correlation function  $C_N(t)$ . To do so, the mean squared change in particle number  $\langle \Delta N^2(t) \rangle$  is subtracted from its plateau, the variance  $\text{Var}(N)$ , as, according to Eq. (2),  $C_N(t) = [\langle \Delta N^2(t) \rangle / 2 - \text{Var}(N)]$ . Again, this highlights that difficulties in resolving  $\text{Var}(N)$  at large length scales have consequences on the accuracy of  $T(L)$ . This is quite apparent in experimental data, especially for the boxes  $L \geq 2\sigma$  in Fig. 5-b, where  $C_N(t)$  does not vanish smoothly. During integration, the decay at long times could be in part improved by replacing the long-time noisy data points with long-time theory-informed extensions, fitted to the experimental data [22]. However, in our experimental system, our dominant limitation is in resolving  $\text{Var}(N)$  and not lack of long-time data (SI Fig. S2). In simulations, the divergence is also not due to lack of data in time, but rather due to periodic boundary conditions which modify collective effects at lengthscales  $L \gtrsim 0.3L_x$ .

Once the correlation function is correctly estimated, one can take its integral, here with trapezoidal integration. For boxes  $L \lesssim 0.3\sigma$ , the correlation function decays so quickly that our imaging timestep can not capture the early time decay, and hence  $T(L)$  is incorrectly estimated. To circumvent this, we match our first experimental data point  $C_N(\Delta t)$  where  $\Delta t = 0.5$  s, is our experimental time, with the short time-small box formula in Eq. (3), and integrate the obtained short time extension over  $[0, \Delta t]$  (see dotted coloured lines in Fig. 5-a and b for  $t \leq 0.5$  s). This short time extension is added on all box sizes but only makes a significant difference on box sizes  $L \lesssim \sigma$  where the decay of the correlation function is otherwise too fast to be captured by data.

*d. Comparison between Methods 1 and 2* We now compare the phenomenological fitting approach of method 1 with the timescale integral approach of method 2. Overall, both methods predict somewhat similar shapes of  $D(L)$  and limiting regimes, which confirms their ability to sense collective effects at a given scale. Both methods can thus characterize collective diffusion dynamics in experimental setups. The results from the phenomenological fit method 1 (Fig. 4-c and d) are more distant to the theory than method 2. This confirms that the timescale integral provides more quantitative insights than the phenomenological fitting. Importantly, the timescale integral method 2 can measure the collective diffusion coefficient  $D_{\text{coll}}$  at large enough lengthscales.

Although method 2 appears more robust, one method might be more convenient than the other in practical situations. Because the phenomenological fit method 1 investigates  $\langle \Delta N^2(t) \rangle$ , it focuses on early to intermediate time scales, requiring somewhat shorter datasets for fitting. However, method 1 works under the assumption of a model. In contrast, method 2 does not require any model *a priori*, and therefore, could suitably be used to infer a relaxation timescale  $T(L)$  of any underlying physical process. The downside is that method 2 requires the long-time decay of the correlation functions to be highly resolved to obtain convergence of the integral. Overall, we find that using both approaches are useful as the point where they differ can serve as an indicator for when the data is not sufficient to obtain accurate predictions.

### III. COMPARISON TO A COMMON FOURIER-BASED APPROACH

At equilibrium, there are several established, albeit potentially difficult to implement, techniques to measure  $D_{\text{coll}}$ . Numerous works rely on probing the diffusion coefficient of the centre of mass  $D_{\text{cm}}$  [1–3, 10, 41, 42]. The collective diffusion is then obtained as  $D_{\text{coll}} = D_{\text{cm}}/S(k=0)$ . Yet, obtaining a statistically meaningful trajectory for the centre of mass requires following a large group of particles for a substantial amount of time, which is experimentally challenging as particles continuously exit and enter the field of view. Even in simulations, only one trajectory is obtained, limiting statistical resolution. Because this technique is essentially impractical and has low statistical resolution, we discard it for benchmarking, and focus on Fourier-based approaches.

#### A. Method 3: Dynamic structure factors

*a. Workflow of method 3.* A common approach to characterize the relaxation of diffusion processes at several scales is to analyze dynamic structure factors  $F(k, t)$  for a given wavenumber  $k$  after a time interval  $t$ . The dynamic structure factor is also referred to

as the intermediate scattering function [8]. Formally, it is defined in Fourier space as the correlation function of the Fourier-transformed densities,  $F(k, t) = \langle \hat{\rho}(\mathbf{k}, t) \hat{\rho}^*(\mathbf{k}, 0) \rangle / N_p$  where  $N_p$  is the number of particles of the suspension. Each particle indexed by  $\mu$  has 2D coordinates given by  $\mathbf{r}_\mu(t) = (x_\mu(t), y_\mu(t))$ , and one can equivalently rewrite

$$F(k, t) = \frac{1}{N_p} \sum_{\mu, \nu=1}^{N_p} \left\langle e^{i\mathbf{k} \cdot (\mathbf{r}_\mu(t) - \mathbf{r}_\nu(0))} \right\rangle \quad (9)$$

where we assumed the system is rotationally invariant such that  $F$  only depends on  $k = |\mathbf{k}|$ . At time zero,  $F$  is equal to the static structure factor  $F(k, t=0) = S(k)$ . Calculating  $F(k, t)$  via Eq. (9) is also called the direct method [43].

The dynamic structure factor  $F(k, t)$  characterizes how the structure of the fluid evolves from a given state. Within linear response, *i.e.* assuming density fluctuations are small, the structural dynamics are fully described by a diffusion coefficient in Fourier space  $D(k, t)$  such that

$$f(k, t) \equiv \frac{F(k, t)}{S(k)} = \exp(-D(k, t)k^2t). \quad (10)$$

Large wavenumbers refer to motion at small scales and hence correspond to individual motion, so we expect  $D(k \gg 1/\sigma, t) = D_{\text{self}}$ . The limit of small wavenumbers in turn describes collective motion, *by definition*,  $D(k \ll 1/\sigma, t) = D_{\text{coll}}$ .

It is important to note that the dynamic structure factor bundles two contributions: correlations between a given particle at a given timepoint and *itself* later in time  $F_s(k, t)$ , and correlations between *distinct* particle at different times  $F_d(k, t)$ . This means  $F(k, t)$  can be rewritten as

$$\begin{aligned} F(k, t) &= F_s(k, t) + F_d(k, t) \\ &= \frac{1}{N_p} \sum_i^{N_p} \left\langle e^{i\mathbf{k} \cdot (\mathbf{r}_i(t) - \mathbf{r}_i(0))} \right\rangle \dots \\ &\quad + \frac{1}{N_p} \sum_{i \neq j}^{N_p} \left\langle e^{i\mathbf{k} \cdot (\mathbf{r}_i(t) - \mathbf{r}_j(0))} \right\rangle. \end{aligned} \quad (11)$$

The relaxation of the self part is entirely dictated by the self diffusion coefficient, as  $F_s(k, t) = \exp(-D_{\text{self}}k^2t)$ .

By inverting the decay of the dynamic structure factor, one can obtain  $D(k, t)$ . So far we have kept a dependence of  $D(k, t)$  on time, yet to simplify data analysis, for now, we will focus on  $D(k) = D(k, t \simeq 0)$ . Generally, data is better resolved at short times, and this justifies our choice. In the SI, we distinguish short and long time regimes, and show similar results overall (SI Fig. S6).

*b. Divergence artefact of method 3, for  $k \rightarrow 0$ .* To make progress on method 3, we work on an example, the dilute suspension at  $\phi = 0.02$ . The dynamic



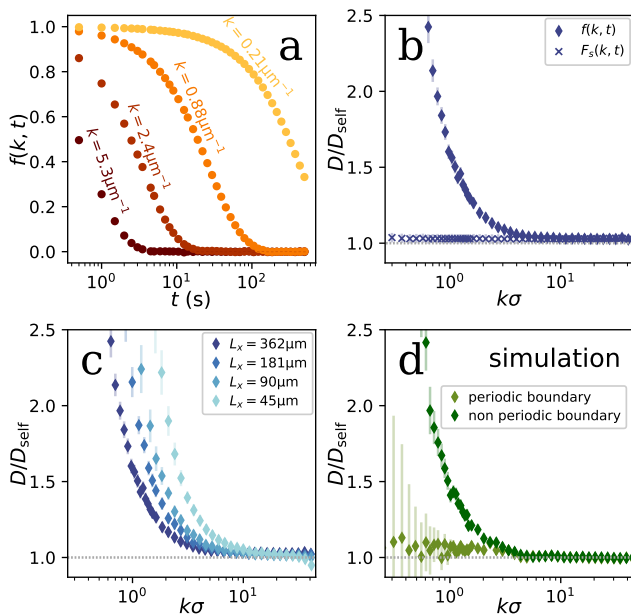


FIG. 6. **Challenges in resolving Fourier space relaxation from experiments at  $\phi = 0.02$ .** (a) Examples of dynamic structure factors  $f(k, t)$  at different wavenumbers  $k$ . (b) Obtained  $D(k)$  from first-point inversion of  $f(k, t)$  and  $F_s(k, t)$ . (c)  $D(k)$  from  $f(k, t)$ , but for cropped microscopy images.  $L_x$  as given in legend,  $L_y$  was picked to preserve aspect ratio of the field of view. (d)  $D(k)$  from  $f(k, t)$  from simulations with periodic and non-periodic boundary conditions. The numerical field of views are taken to be the same size. This subplot is repeated for the dense case in SI Fig. S8

structure factor  $f(k, t)$  is first computed via Eq. (9) at various wavelengths  $k$  (Fig. 6-a). To extract the scale-dependent diffusion coefficient  $D(k)$ , we invert Eq. (10) at the first (non zero) time point. The obtained  $D(k)$  for all relevant wavelengths for the dilute suspension is presented in Fig. 6-b (diamonds). Surprisingly, for this dilute suspension we notice a clear divergence at small wavelengths of  $D(k)$ . Note that this divergence is not visible in the self diffusion coefficient  $D_{\text{self}}$  extracted in a similar way from  $F_s(k, t)$  (Fig. 6-b, crosses). We do not expect such changes in the collective diffusion coefficient  $D(k \rightarrow 0)$  for such a dilute suspension.

To unravel the origin of this peculiar artefact, we conduct the analysis again on modified versions of the experimental data. First, we trim the duration of our experimental data, and plot  $D(k)$  for different trimmed lengths, and find no significant difference (see SI Fig. S7). The artefact is thus not due to a lack of statistics. Second, we crop experimental movies, effectively reducing the effective field of view ( $L_x, L_y$ ). The divergence in  $D(k)$  is significantly affected by cropping: occurring at larger wavenumbers for smaller images, see Fig. 6-c. Typically, the divergence starts for  $k$  values such that  $k \lesssim 2\pi/(L_x/10)$ . This hints that the

artefact originates from edge effects. Finally, we also compute  $D(k)$  from simulation data, see Fig. 6-d (light green), and do not find the divergence.

The fundamental difference between experiments and simulations is that the simulated data has periodic boundary conditions. To mimic the experimental situation, we run a simulation on a much larger simulation box and do the  $D(k)$  analysis on a cropped subset of the data, see Fig. 6-d (dark green). Under these simulated non-periodic boundary conditions, we recover a similar divergence in  $D(k)$  as found experimentally. This demonstrates that the absence of periodic boundary conditions is at the origin of the artefact. The resolution of the dynamic structure factor is thus intrinsically limited by the finite field of view of the experiment.

While a detailed investigation of why this artefact appears is beyond the scope of this work, edge effects are its roots. Such edge effects are common on Fourier transforms of images, where numerous techniques have been developed to limit related artefacts [27, 29]. Such techniques are not directly applicable to discrete particle positions, and hence to the computation of  $F(k, t)$  via Eq. (9), yet motivate perspectives for improvement. To conclude this investigation, we simply raise caution and stress that the relevant values of  $k$  to observe dynamic behaviour over should be taken such that  $2\pi/k \lesssim 0.1L_x$  for experimental data with observation windows  $L_x$ .

*c. Results for  $D(k)$  in a dense suspension.* We can now investigate the wave-number dependent  $D(k)$  for the dense suspension  $\phi = 0.11$ . To relate to our previous results obtained via the Countoscope, we present data as  $D(k = 2\pi/L)$ , effectively flipping the x axis horizontally, see Fig. 7. The divergence artefact occurs on experimental data, both for  $\phi = 0.11$  and  $\phi = 0.02$  around similar lengthscales, beyond which we raise caution on over-interpretation of the data (Fig. 7-b). Nonetheless, distinct features appear in  $D(k)$  at this higher packing fraction. In particular, we notice a minimum in  $D(k)$  around  $L \simeq \sigma$ . The scale-dependent diffusion coefficient  $D(k)$  is quite sensitive to the fluid's structure at different wavelengths, as we expect  $D(k) \sim 1/S(k)$ . The maximum in  $S(k)$  (see Fig. IV 0 d), corresponding to ordering at increased packing fractions, thus corresponds with a minimum in  $D(k)$ , the so-called De Gennes narrowing [44]. This interpretation can be checked by overlapping the theoretical prediction  $D(k) = D_{\text{self}}/S(k)$  on simulation and experiments (black line in Fig. 7), where  $S(k)$  is given by Eq. (28) (Appendix D). The minimum in  $D(k)$  is faithfully captured by this theoretical expression, confirming the presence of De Gennes narrowing. Simulations without hydrodynamics perfectly reproduce the theory, and plateau to the collective diffusion coefficient  $D_{\text{coll}}$  as expected, confirming the validity of our analysis scheme.

In contrast, sharp discrepancies arise between experimental data and theory, for large wavelengths  $L \gtrsim 2 - 3\sigma$ , which are usually attributed to hydrodynamic

corrections [18–20]. Unfortunately, such discrepancies also arise where the divergence artefact in  $D(k)$  kicks in. These divergences also occur for wavelengths that are smaller than the critical wavelength to reach the  $D_{\text{coll}}$  plateau, which would require  $L \gtrsim 10\sigma$ . To deconvolve hydrodynamic contributions from this artefact is beyond the scope of our work. Yet, several strategies are worth mentioning. On the experimental side, one could use wider fields of view to increase the range of relevant  $L$  lengths or design de-aliasing techniques [27, 29]. Simulations including hydrodynamic lubrication between particles could be conducted [22, 34] and compared with simulations with purely steric interactions as well, but require intense computational resources: only long simulation timescales and wide simulation boxes can resolve decorrelation accurately at these large wavelengths.

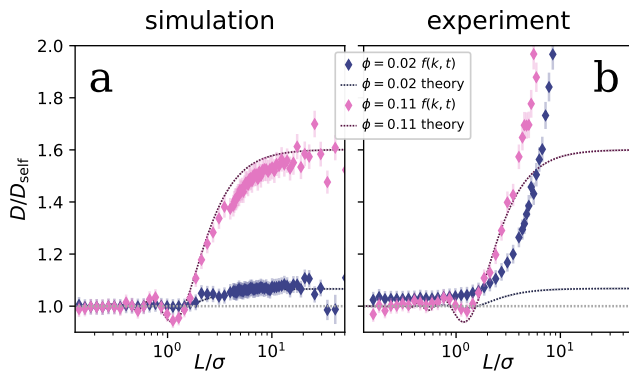


FIG. 7. **Method 3: Relaxation of dynamic structure factors.**  $D(L = 2\pi/k)$  for  $\phi = 0.02$  (blue) and  $\phi = 0.11$  (pink) obtained from short time analysis of the dynamic structure factor in (a) simulations and (b) experiments. Theory lines correspond with  $D(k) = D_{\text{self}}/S(k)$  with  $S(k)$  given in Eq. (28). The divergence for  $L \gtrsim 2 - 3\sigma$  in (b) corresponds to non-periodic boundaries as discussed in Fig. 6 and in the text.

### B. Comparison of collective diffusion properties as probed in Counting versus Fourier space

The features observed in  $D(k = 2\pi/L)$  via the investigation of the dynamic structure factor are reminiscent of features of  $D(L)$  inferred from the Countoscope. We compare these in more detail now, by overlapping  $D(k)$  and  $D(L)$  for simulations and experiments in the dense regime  $\phi = 0.11$  (Fig. 8). Overall, the fluid’s structure is quite apparent on  $D(k)$ , and less so on  $D(L)$ . Curiously the maximum in  $D(L)$  occurs at a similar lengthscale to the minimum in  $D(k)$ , a behaviour which would require further investigation at different packing fractions to be confirmed. The increase in the scale-dependent diffusion coefficient occurs at different scales: counting is sensitive to collective effects

typically for  $L \gtrsim \sigma$  while one must wait for  $L \gtrsim 5\sigma$  for collective effects in  $D(k)$ , demonstrating the sensitivity of counting.

Based on simulation data, we find counting can estimate the collective diffusion coefficient  $D_{\text{coll}}$  on large boxes. Indeed, in Fig. 8-a, we observe  $D(k \rightarrow 0) = D(L \rightarrow \infty) = D_{\text{coll}} = D_{\text{self}}/S(k = 0)$ . The measurement of the collective diffusion coefficient  $D_{\text{coll}}$  via the Countoscope or the dynamic structure factor approach are thus equal. As a periodic methodology, the Fourier-based approach on simulation data appears to diverge less at large length-scales, compared to the Countoscope. Nonetheless, one should keep in mind that finite-simulation size effects can still affect the plateau reached by  $D(k)$  significantly (SI Fig. S5).

In experiments, it is hard at this stage to compare the limiting behaviour of  $D(L)$  and  $D(k)$  for  $L \rightarrow \infty$  or  $k \rightarrow 0$  due to the artefact divergence in  $D(k)$ . However, in experiments, counting provides information on  $D(L)$  at much larger lengthscales than  $D(L)$ . As a real-space methodology, counting is more robust on non-periodic experimental data than Fourier-based approaches.

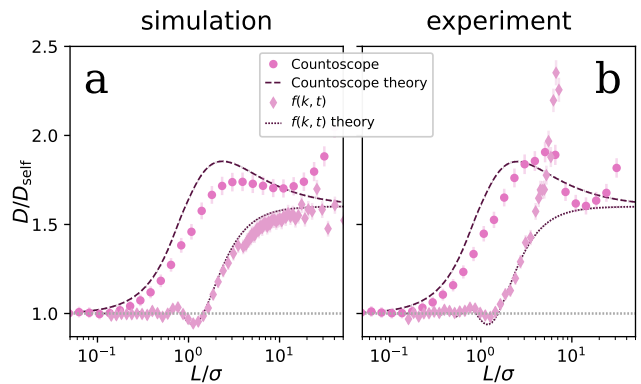


FIG. 8. **Comparison of Countoscope versus Fourier-space approaches:** via  $D(L)$  computed via the timescale integral method 2 (dots) and  $D(k = 2\pi/L)$  computed via the early-time fit of the dynamic structure factor (diamonds), for (a) simulations and (b) experiments for the intermediate packing fraction  $\phi = 0.11$ . Theory lines correspond with Eq. (8) for the Countoscope and  $D(k) = D_{\text{self}}/S(k)$  with  $S(k)$  given in Eq. (28) for the Fourier approach.

## IV. DISCUSSION AND CONCLUSION

In this work, we have shown how to infer collective diffusion properties at various spatial lengthscales by counting particles in boxes. The box-size dependent diffusion coefficient  $D(L)$  can be obtained via time integration of the correlation function of particle numbers in a box  $\langle N(t)N(0) \rangle$ , or via phenomenological fits of number fluctuations.  $D(L)$  converges to the self diffusion coefficient  $D_{\text{self}}$  in small boxes. In large boxes,  $D(L) \rightarrow$

$D_{\text{coll}}$ , as confirmed via theory, simulations and Fourier-based approaches of the dynamic structure factor. We have found Fourier approaches struggle with the finite field of view of microscopy images, leading to unphysical divergences of  $D(L)$  at large wavelengths. In contrast, counting exploits finite fields of view by deliberately paving the image with finite observation boxes. Finally,  $D(L)$  informs on collective dynamics at all spatial scales  $L$ , allowing us to broadly investigate collective properties of suspensions.

We anticipate that our method could shed light on the effect of hydrodynamic interactions in colloidal suspensions, in particular for quasi 2D suspensions near walls, which occur quite commonly in soft matter systems. Previous theoretical and experimental investigations of quasi 2D geometries have suggested that long-range correlations between particles can enhance collective motion dramatically, resulting in a divergence of  $D(k)$  at large wavelengths [17–21, 48–50]. This is at odds with bulk 3D systems, where hydrodynamic interactions reduce the value of  $D_{\text{coll}}$  [15–17]. Interestingly, we find in our experimental data that a divergence on  $D(k)$  is linked to edge effects, and thus potential effects of hydrodynamic interactions are hidden. In contrast, on experimental data, we appear to reach a plateau in  $D(L)$  with our Countoscope approach, at least over a certain range of length scales. Our experimental data suggests a limiting  $D_{\text{coll}}$  which is only slightly higher than the one described by simulations or theory without hydrodynamic interactions. Beyond this artefact divergence, which could also be at play in previous works, discrepancies could originate from diverse physical factors. At higher packing fractions, up to  $\phi \simeq 0.6$ , we expect hydrodynamic effects could be more important [22]. The geometry of our system consists of particles at a single wall as opposed to a fluid-fluid interface or between two closely-spaced walls [17–21, 48], and geometry is known to significantly influence the range over which hydrodynamic interactions decay [51, 52]. The decay of hydrodynamic interactions could be a transient short-time effect, requiring further interpretation of  $D_{\text{coll}}$  as a time-dependent property [12]. Generally, we stress that to obtain accurate quantification of collective properties, significant data sets are required, both in time and spatially: our experimental data sets are 100 times larger than the particle size, and more than 1000 times longer than the time to diffuse across a particle’s diameter and only nearly capture  $D_{\text{coll}}$ . The counting recipe provides further tools to investigate collective phenomena, and understand the effects of hydrodynamic interactions in various geometries.

To investigate collective effects, it is clear that, regardless of the method, wide fields of view are necessary to resolve motion at large spatial scales. Especially in dense systems where collective effects arise, this means that trajectory reconstruction may no longer be feasible [32, 53, 54]. For the investigation of

collective effects, this is not an issue as both counting or dynamic structure factors  $F(k, t)$  do not require trajectories (Table I). In that sense, counting fills a gap in the field, as the real-space equivalent of  $F(k, t)$ . Density fluctuations are also investigated in real space through intensity fluctuations of scattered light, via Fluorescence Correlation Spectroscopy [45] or Dynamic Light Scattering [46]. In contrast with these techniques, we explicitly count numbers, avoiding the link between scattered intensities and particle numbers which is especially ambiguous at high densities [55, 56]. More importantly, the Countoscope is not restricted to a given lengthscale, unlike *e.g.* FCS which analyzes the scattered light of a given illuminated region. This suggests exploring intensity correlations in real space on virtual boxes of an image, a form of “intensity Countoscope”. Again, this would fill a gap in the field, as the real space equivalent of Differential Dynamic Microscopy [47].

More generally, we hypothesize that probing number correlations at different scales could inform us about more diverse collective transport properties, beyond diffusion. For instance, in active matter systems, either synthetic or biological, peculiar features are common in static number fluctuations: “Giant” number fluctuations, where  $\alpha > 0$  in the scaling  $\langle N^2 \rangle - \langle N \rangle^2 \sim N^{1+\alpha}$ , indicate long-range organization, as found in bacterial aggregates and active matter [57–65]. Likely, investigating the dynamic counterpart of these static fluctuations, through the decorrelation time  $T(L)$  of number fluctuations at different scales could help us characterize collective motile states, and perhaps shed light on how they emerge from specific interparticle interactions [6, 7].

## DATA AVAILABILITY

All data needed to evaluate the conclusions in the paper are present in the paper and/or the Supplementary Materials. All other data are available upon reasonable request to the authors.

## ACKNOWLEDGEMENTS

We wish to acknowledge fruitful discussions with Jean-Louis Barrat, Roxanne Berthin, Ludovic Berthier, Roberto Cerbino, Benoit Coasne, Rafael Delgado Buscalioni, Aleksandar Donev, Simon Gravelle, Pierre Levitz, Grace Mattingly, Amaël Obliger and Alexander Schlaich.

Financial support for this project was provided by the Institute of Materials Science (iMAT) of the Alliance Sorbonne Université. A.C. acknowledges iMAT for a PhD grant. A.L.T. acknowledges funding from a Royal Society University Research Fellowship (URF\R1\211033). E.K.R.M. and A.L.T. acknowledge funding from EPSRC (EP/X02492X/1).

	scattering	microscopy		
	intensities	intensities	positions	trajectories
Real-space	FCS [45], DLS [46]	Intensity Counting	Countoscope [22]	MSD
Fourier-space	XPCS, DLS [46]	DDM [47]	$F(k, t)$	$F_s(k, t), F_d(k, t)$

TABLE I. Comparison of different techniques for analyzing particle dynamics in scattering and microscopy experiments.

B.S. acknowledges funding from the National Science Foundation award DMS-2052515.

### AUTHOR CONTRIBUTIONS

The authors confirm their contribution to the paper as follows: study conception and design: S.M.; simulation data collection: A.C.; simulation design: A.C., B.S.; experimental data collection: E.K.R.M.; experimental design: E.K.R.M., A.L.T., modeling: A.C., S.M.; data analysis: A.C.; data interpretation: A.C., B.S., A.L.T., S.M.; visualization: A.C.; draft manuscript preparation: A.C., S.M.; review and editing: A.C., A.L.T., S.M.

### COMPETING INTERESTS

The authors declare no competing interests.

### APPENDIX

#### APPENDIX A: METHODOLOGICAL DETAILS

*a. Experiments.* Carboxylate-functionalised melamine formaldehyde particles (Microparticles GmbH) are dispersed in 20/80 v/v% ethanol-water mixtures, and suspensions are loaded into quartz glass flow cells. Particle diameters are characterised by fitting hard-disk DFT results [30] to the experimental structure factor (see Fig. IV 0 d). The particles' high mass density ( $\rho = 1510 \text{ kg m}^{-3}$ ) means they sediment rapidly to the base of the sample cell to form a monolayer, and further that the gravitational height is small ( $\approx 0.02\sigma$ ) so out-of-plane fluctuations are negligible. Due to this close confinement, the particles interact hydrodynamically with the base of the flow cell, but interactions with the upper surface are not significant as this is separated by a height of  $\approx 70\sigma$  from the plane of the particles. Microscope images provide a  $390 \times 295 \mu\text{m}^2$  field of view,  $\sim 10^{-6}$  times smaller than the total sample cell area. We ignore any interactions with the flow cell side walls.

Data sets are checked for systematic drift in particle positions or image packing fraction over the course of the experiments.

*b. Simulations.* Simulations were performed as described in Ref. [22]. The simulation box was of side length  $640 \mu\text{m}$  except where specified, and particle diameter  $3.0 \mu\text{m}$ . Particle trajectories are wrapped with periodic boundary conditions in  $x$  and  $y$ . Simulations were run twice, once with data being saved for analysis with a timestep of 0.5 s and simulated time 22 hours, and subsequently with a timestep of 16 s and simulated time of 710 hours. Data from the short runs were used to compute  $D$  for short length scales ( $L < \sigma$  and  $k > 1.8/\sigma$ ), and data from the long runs used to compute  $D$  for large length scales. As we compute  $D(k)$  from inverting the first non-zero time point of  $f(k, t)$  (see Sec. III A 0 b), for small  $k$  we are probing  $D(k, 0.5 \text{ s})$ , but for large  $k$  we are probing  $D(k, 16 \text{ s})$ . This is the source of the small discontinuity visible on Fig. 7 at  $L/\sigma = 3.5$ .

*c. Calculation of dynamic structure factors.* We give further details on how we compute  $f(k, t)$ . First, Eq. (9) is extended to 2-time points with non-constant  $N_p$  particles, as particle numbers in experiments are not conserved over time. We take the normalizing factor as the average over the 2 time points,  $N_p = (N_p(0) + N_p(t))/2$ , and the sum runs over all particles at each time frame. The dynamic structure factor is first computed via Eq. (9) over a 2D grid of  $k$  vectors as  $F(k_x, k_y, t)$ . The 2D wavenumbers are taken along a regular grid for  $k \leq 0.5 \mu\text{m}^{-1}$ :  $(k_x, k_y) = (n2\pi/L_x, m2\pi/L_y)$  where  $(L_x, L_y)$  is the size of the optical image and  $n, m$  are integers. For  $k > 0.5 \mu\text{m}^{-1}$  we find the result to be unaffected by the grid spacing, so we space the grid logarithmically to reduce computational expense. The wavevector magnitude is then calculated as  $k = \sqrt{k_x^2 + k_y^2}$ , and a radial average is performed by binning the values of  $k$  and  $F$  with bins spaced as above, and their final values are taken as the mean of their respective values in each bin.

## APPENDIX B: COUNTS IN LARGE BOXES PROBE COLLECTIVE PROPERTIES

In Ref. [22], we established that the 2D number fluctuations of hard spheres can be described via the equation

$$C_N(t) = \langle N \rangle \int \frac{k dk}{(2\pi)^2} L^2 f_V(k) S(k) e^{-D_{\text{self}} k^2 t / S(k)} \quad (12)$$

where  $f_V(k)$  is a characteristic non dimensional geometrical factor depending on the wavenumber amplitude only

$$f_V(k) = \int d\theta \left( \frac{\sin(k_x(\theta)L/2)}{k_x(\theta)L/2} \right)^2 \left( \frac{\sin(k_y(\theta)L/2)}{k_y(\theta)L/2} \right)^2 \quad (13)$$

with  $k_x(\theta) = k \cos \theta$  and  $k_y(\theta) = k \sin \theta$ ; and  $S(k)$  is the structure factor of the fluid.

Our goal here is to show Eq. (12) converges to the limiting regimes Eq. (3) and (5) in the limit of small and large boxes respectively. To do so, we first introduce the non-dimensional wavenumber  $K = kL/2$  such that the geometrical factor becomes

$$f_V(K) = \int d\theta \left( \frac{\sin(K \cos \theta)}{K \cos \theta} \right)^2 \left( \frac{\sin(K \sin \theta)}{K \sin \theta} \right)^2 \quad (14)$$

and the correlation function

$$C_N(t) = \langle N \rangle \int \frac{K dK}{(\pi)^2} f_V(K) S \left( \frac{2K}{L} \right) \times \dots \quad (15)$$

$$e^{-(4D_{\text{self}} t / L^2) \times K^2 / S(2K/L)}.$$

It is then useful to approximate the structure factor  $S(k)$  in the following way. Typically, when  $k \geq 1/\sigma$ ,  $S(k) \simeq 1$  and when  $k \leq 1/\sigma$ , then  $S(k) \simeq S(k=0)$ . This means we can split the above integral in 2 distinct contributions

$$C_N(t) = \langle N \rangle \int_{L/2\sigma}^{\infty} \frac{K dK}{(\pi)^2} f_V(K) e^{-\frac{4D_{\text{self}} t}{L^2} K^2} + \quad (16)$$

$$\langle N \rangle S(0) \int_0^{L/2\sigma} \frac{K dK}{(\pi)^2} f_V(K) e^{-\frac{4D_{\text{self}} t}{S(0)L^2} K^2}.$$

It is then rather straightforward to look at the two limiting cases of small and large box. If  $L \lesssim \sigma$ , then  $L/\sigma \lesssim 1$ . Clearly, the 2nd integral in Eq. (16) is negligible, and one can assume  $\int_{L/2\sigma}^{\infty} \simeq \int_0^{\infty}$ . We arrive at an expression corresponding to the 2D case without interactions, where the integral over  $K$  can be conducted, and

$$C_N(t) = \langle N \rangle \left[ f \left( \frac{4D_{\text{self}} t}{L^2} \right) \right]^2, \quad (17)$$

where  $f$  is defined in Eq. (3). Using Eq. (2), one directly arrives at Eq. (3) in the main text.

In contrast, when  $L \gtrsim \sigma$ , then  $L/\sigma \gtrsim 1$ . In that case, the 1st integral in Eq. (16) becomes negligible and we

can assume  $\int_0^{L/2\sigma} \simeq \int_0^{\infty}$ . We also arrive at an expression corresponding to the 2D case without interactions, but this time  $D_{\text{self}} \rightarrow D_{\text{self}}/S(0)$  and the prefactor  $S(0)$  is in front of the integration sign. This means we obtain

$$C_N(t) = \langle N \rangle S(0) \left[ f \left( \frac{4D_{\text{self}} t}{S(0)L^2} \right) \right]^2. \quad (18)$$

Since  $D_{\text{coll}} = D_{\text{self}}/S(0)$ , we can replace it in the expression above. In addition, because  $C_N(0) = \text{Var}(N)$ , and  $f(0) = 1$ , one sees that in the limit of large boxes  $L \gtrsim \sigma$

$$\text{Var}(N) \simeq \langle N \rangle S(0) \quad (19)$$

such that for large boxes we arrive at

$$C_N(t) = \text{Var}(N) \left[ f \left( \frac{4D_{\text{coll}} t}{L^2} \right) \right]^2, \quad (20)$$

and using Eq. (2), we recover Eq. (5) of the main text.

Finally, one can also notice that for small boxes  $L \lesssim \sigma$ , based on Eq. (17),

$$\text{Var}(N) \simeq \langle N \rangle \quad (21)$$

which justifies the phenomenological scaling law Eq. (6) in the main text.

*d. Timescale integrals* Given the expression of the timescale integral in Eq. (7), it is then straightforward, with Eq. (17), to show that in the limit of small boxes,

$$T(L) = \alpha_T \frac{L^2}{4D_{\text{self}}} \text{ where } \alpha_T = \int_0^{\infty} f(\tau)^4 d\tau. \quad (22)$$

Similarly, in the limit of large boxes, one arrives at a similar expression

$$T(L) = \alpha_T \frac{L^2}{4D_{\text{coll}}} \quad (23)$$

and hence we obtain the following Countscope limits

$$D(L \lesssim \sigma) \rightarrow D_{\text{self}}, \quad D(L \gtrsim \sigma) \rightarrow D_{\text{coll}}. \quad (24)$$

## APPENDIX C: WAVENUMBER DEPENDENT $D(k)$ PREDICTIONS

We here show that we expect  $D(k) = D_{\text{self}}/S(k)$  within the theory we used to investigate hard sphere dynamics. The first step is to notice that the correlation function is obtained from integrating the density correlation function in Fourier space, as

$$C_N(t) = \int_{[-\frac{L}{2}, \frac{L}{2}]^2} d\mathbf{r} d\mathbf{r}' \langle (\rho(\mathbf{r}, t) - \rho_0)(\rho(\mathbf{r}', 0) - \rho_0) \rangle,$$

$$= \rho_0 \int_{[-\frac{L}{2}, \frac{L}{2}]^2} d\mathbf{r} d\mathbf{r}' \int \frac{d\mathbf{k}}{(2\pi)^2} e^{i\mathbf{k} \cdot (\mathbf{r} - \mathbf{r}')} F(\mathbf{k}, t).$$

Going back to cartesian coordinates, with  $k_x(\theta) = k \cos \theta$  and  $k_y(\theta) = k \sin \theta$ , and integrating over the box gives

$$\begin{aligned} C_N(t) &= \int_{[-\frac{L}{2}, \frac{L}{2}]^2} dx dy dx' dy' \times \dots \\ &\int \frac{k dk d\theta}{(2\pi)^2} e^{ik_x(\theta)(x-x')} e^{ik_y(\theta)(y-y')} F(k, t) \\ &= \rho_0 L^4 \int \frac{k dk}{(\pi)^2} f_V(k) F(k, t), \end{aligned}$$

where  $f_V(k)$  is defined in Eq. (13). Given that  $\langle N \rangle = \rho_0 L^2$ , we can identify terms with Eq. (12), and find

$$F(k, t) = S(k) e^{-D_{\text{self}} k^2 t / S(k)}. \quad (25)$$

Note that expression is only valid within an approximation of *small* density fluctuations – a linearization of the so-called Dean Kawasaki equation [35, 36], which is the starting point of our theory. Other approaches also stress that this is a linear approximation [8]. It is then straightforward to identify from Eq. (9):

$$D(k, t) = \frac{D_{\text{self}}}{S(k)}. \quad (26)$$

Note that within this approximation,  $D(k, t)$  does not depend on time, and we can simply write  $D(k)$ .

#### APPENDIX D: STATIC STRUCTURE FACTOR

In Eq. (12) and onwards we use an analytic expression for the structure factor of hard spheres in 2D, which is based on density field theory and is in remarkable agreement with our 2D-sedimented colloidal experiments, as was verified in a previous work [66] and can be seen in Fig. IV 0d. We report it here for consistency:

$$S(k) = \frac{1}{1 - \rho c^{(2)}(k)} \quad (27)$$

where  $\rho$  is the mean particle density and

$$\begin{aligned} c^{(2)}(k) &= \frac{\pi}{6(1-\phi)^3 k^2} \left[ -\frac{5}{4}(1-\phi)^2 k^2 \sigma^2 J_0(k\sigma/2)^2 \right. \\ &\quad + \left( 4((\phi-20)\phi + 7) \right. \\ &\quad + \left. \frac{5}{4}(1-\phi)^2 k^2 \sigma^2 \right) J_1(k\sigma/2)^2 \\ &\quad \left. + 2(\phi-13)(1-\phi)k\sigma J_1(k\sigma/2)J_0(k\sigma/2) \right] \quad (28) \end{aligned}$$

where  $J_i(x)$  are Bessel functions of the first kind. The limit of vanishing wavenumber in Eq. (28) can be taken analytically

$$S(k=0) = \frac{(1-\phi)^3}{1+\phi} \quad (29)$$

and is consistent with the result from the scaled particle theory equation of state.

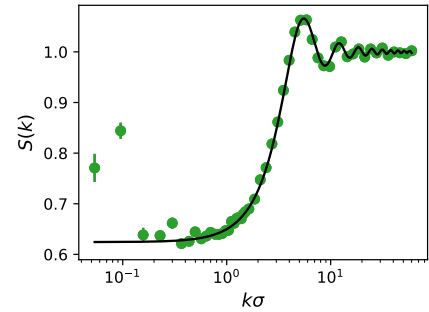


FIG. 9.  $S(k)$  for experimental data at packing fraction  $\phi = 0.11$  (green). Black curve is a fit to Eq. 27 where the particle diameter  $\sigma$  is the only adjustable parameter. We find  $\sigma = 3.0 \mu\text{m}$ .

- 
- [1] K. Ariskina, G. Galliéro, and A. Obliger, Free volume model for transport in flexible kerogen of source rock's organic matter, *The Journal of Physical Chemistry B* **126**, 7409 (2022).
  - [2] A. Obliger, R. Pellenq, F.-J. Ulm, and B. Coasne, Free volume theory of hydrocarbon mixture transport in nanoporous materials, *The Journal of Physical Chemistry Letters* **7**, 3712 (2016).
  - [3] K. Falk, B. Coasne, R. Pellenq, F.-J. Ulm, and L. Bocquet, Subcontinuum mass transport of condensed hydrocarbons in nanoporous media, *Nature communications* **6**, 6949 (2015).
  - [4] M. E. Cates and J. Tailleur, Motility-induced phase separation, *Annu. Rev. Condens. Matter Phys.* **6**, 219 (2015).
  - [5] B. Liebchen, D. Marenduzzo, and M. E. Cates, Phoretic interactions generically induce dynamic clusters and wave patterns in active colloids, *Physical review letters* **118**, 268001 (2017).
  - [6] B. Liebchen and A. K. Mukhopadhyay, Interactions in active colloids, *Journal of Physics: Condensed Matter* **34**, 083002 (2021).
  - [7] M. Dijkstra and E. Luijten, From predictive modelling to machine learning and reverse engineering of colloidal self-assembly, *Nature materials* **20**, 762 (2021).
  - [8] J. K. Dhont, *An introduction to dynamics of colloids* (Elsevier, 1996).
  - [9] A. Einstein, Über die von der molekularkinetischen theorie der wärme geforderte bewegung von in ruhenden flüssigkeiten suspendierten teilchen, *Annalen der physik*

- 4 (1905).
- [10] A. Schlaich, J.-L. Barrat, and B. Coasne, Theory and modeling of transport in nanoporous materials: From microscopic to coarse-grained descriptions, arXiv preprint arXiv:2406.03039 (2024).
- [11] R. Gomer, Diffusion of adsorbates on metal surfaces, Reports on progress in Physics **53**, 917 (1990).
- [12] S. Panzuela and R. Delgado-Buscalioni, Solvent hydrodynamics enhances the collective diffusion of membrane lipids, Phys. Rev. Lett. **121**, 048101 (2018).
- [13] S. Panzuela, R. P. Peláez, and R. Delgado-Buscalioni, Collective colloid diffusion under soft two-dimensional confinement, Phys. Rev. E **95**, 012602 (2017).
- [14] M. Kops-Werkhoven and H. Fijnaut, Dynamic behavior of silica dispersions studied near the optical matching point, The Journal of Chemical Physics **77**, 2242 (1982).
- [15] X. Qiu, X. Wu, J. Xue, D. Pine, D. Weitz, and P. M. Chaikin, Hydrodynamic interactions in concentrated suspensions, Physical review letters **65**, 516 (1990).
- [16] B. O. P. Segrè, P. N. and P. N. Pusey, Short-time brownian motion in colloidal suspensions: Experiment and simulation, Physical Review E **52**, 5070 (1995).
- [17] J. Bleibel, A. Domínguez, and M. Oettel, 3D hydrodynamic interactions lead to divergences in 2D diffusion, J. Phys.: Condens. Matter **27**, 194113 (2015).
- [18] B. Lin, S. A. Rice, and D. A. Weitz, Experimental evidence for the divergence of a transport coefficient in a quasi-two-dimensional fluid, Phys. Rev. E **51**, 423 (1995).
- [19] B. Lin, B. Cui, X. Xu, R. Zangi, H. Diamant, and S. A. Rice, Divergence of the long-wavelength collective diffusion coefficient in quasi-one- and quasi-two-dimensional colloidal suspensions, Phys. Rev. E **89**, 022303 (2014).
- [20] J. Bleibel, A. Domínguez, F. Günther, J. Harting, and M. Oettel, Hydrodynamic interactions induce anomalous diffusion under partial confinement, Soft Matter **10**, 2945 (2014).
- [21] E. Falck, J. M. Lahtinen, I. Vattulainen, and T. Ala-Nissila, Influence of hydrodynamics on many-particle diffusion in 2D colloidal suspensions, Eur. Phys. J. E **13**, 267 (2004).
- [22] E. K. R. Mackay, S. Marbach, B. Sprinkle, and A. L. Thorneywork, The countoscope: Measuring self and collective dynamics without trajectories, Phys. Rev. X **14**, 041016 (2024).
- [23] C. Loussert, A. Bouchaudy, and J.-B. Salmon, Drying dynamics of a charged colloidal dispersion in a confined drop, Physical Review Fluids **1**, 084201 (2016).
- [24] C. Keita, Y. Hallez, and J.-B. Salmon, Microfluidic osmotic compression of a charge-stabilized colloidal dispersion: Equation of state and collective diffusion coefficient, Physical Review E **104**, L062601 (2021).
- [25] B. Sobac, S. Dehaeck, A. Bouchaudy, and J.-B. Salmon, Collective diffusion coefficient of a charged colloidal dispersion: interferometric measurements in a drying drop, Soft matter **16**, 8213 (2020).
- [26] A. Merlin, J. Angly, L. Daubersies, C. Madeira, S. Schöder, J. Leng, and J. B. Salmon, Time-resolved microfocused small-angle x-ray scattering investigation of the microfluidic concentration of charged nanoparticles, The European Physical Journal E **34**, 1 (2011).
- [27] L. Moisan, Periodic plus smooth image decomposition, Journal of Mathematical Imaging and Vision **39**, 161 (2011).
- [28] F. Giavazzi, P. Edera, P. J. Lu, and R. Cerbino, Image windowing mitigates edge effects in differential dynamic microscopy, The European Physical Journal E **40**, 1 (2017).
- [29] A. Zuccolotto-Bernez, L. Rojas-Ochoa, S. Egelhaaf, and M. Escobedo-Sánchez, Improving data sampling with rapid statistical convergence in digital fourier microscopy analysis, Applied Optics **63**, 8760 (2024).
- [30] A. L. Thorneywork, R. Roth, D. G. A. L. Aarts, and R. P. A. Dullens, Communication: Radial distribution functions in a two-dimensional binary colloidal hard sphere system, The Journal of Chemical Physics **140**, 161106 (2014).
- [31] A. L. Thorneywork, R. E. Rozas, R. P. Dullens, and J. Horbach, Effect of Hydrodynamic Interactions on Self-Diffusion of Quasi-Two-Dimensional Colloidal Hard Spheres, Phys. Rev. Lett. **115**, 268301 (2015).
- [32] J. C. Crocker and D. G. Grier, Methods of Digital Video Microscopy for Colloidal Studies, Journal of Colloid and Interface Science **179**, 298 (1996).
- [33] D. B. Allan, T. Caswell, N. C. Keim, C. M. van der Wel, and R. W. Verweij, soft-matter/trackpy: Trackpy v0.5.0 (2021).
- [34] B. Sprinkle, E. B. Van Der Wee, Y. Luo, M. M. Driscoll, and A. Donev, Driven dynamics in dense suspensions of microrollers, Soft Matter **16**, 7982 (2020).
- [35] D. S. Dean, Langevin equation for the density of a system of interacting langevin processes, Journal of Physics A: Mathematical and General **29**, L613 (1996).
- [36] K. Kawasaki, Stochastic model of slow dynamics in supercooled liquids and dense colloidal suspensions, Physica A: Statistical Mechanics and its Applications **208**, 35 (1994).
- [37] T. H. N. Minh, B. Rotenberg, and S. Marbach, Ionic fluctuations in finite volumes: fractional noise and hyperuniformity, Faraday Discussions 10.1039/D3FD00031A (2023).
- [38] J.-P. Hansen and I. R. McDonald, *Theory of simple liquids: with applications to soft matter* (Academic press, 2013).
- [39] E. K. Mackay, A. Young, A. Carter, S. Marbach, and A. L. Thorneywork, Low frequency noise is governed by return kinetics in interacting particle systems, to appear (2024).
- [40] B. Efron, Bootstrap methods: another look at the jackknife, in *Breakthroughs in statistics: Methodology and distribution* (Springer, 1992) pp. 569–593.
- [41] T. Ala-Nissila, R. Ferrando, and S. Ying, Collective and single particle diffusion on surfaces, Advances in Physics **51**, 949 (2002).
- [42] A. Thorneywork, *Structure and dynamics of two-dimensional colloidal hard spheres*, Ph.D. thesis, University of Oxford (2015).
- [43] F. Sedlmeier, D. Horinek, and R. R. Netz, Spatial Correlations of Density and Structural Fluctuations in Liquid Water: A Comparative Simulation Study, J. Am. Chem. Soc. **133**, 1391 (2011).
- [44] W. Kellouai, J.-L. Barrat, P. Judeinstein, M. Plazenet, and B. Coasne, On de gennes narrowing of fluids confined at the molecular scale in nanoporous materials, The Journal of Chemical Physics **160**, 10.1063/5.0186956 (2024).
- [45] E. L. Elson and D. Magde, Fluorescence correlation spectroscopy. i. conceptual basis and theory,

- Biopolymers: Original Research on Biomolecules **13**, 1 (1974).
- [46] B. J. Berne and R. Pecora, *Dynamic light scattering: with applications to chemistry, biology, and physics* (Courier Corporation, 2000).
- [47] R. Cerbino and V. Trappe, Differential Dynamic Microscopy: Probing Wave Vector Dependent Dynamics with a Microscope, *Phys. Rev. Lett.* **100**, 188102 (2008).
- [48] R. P. Peláez, F. B. Usabiaga, S. Panzuela, Q. Xiao, R. Delgado-Buscalioni, and A. Donev, Hydrodynamic fluctuations in quasi-two dimensional diffusion, *J. Stat. Mech.* **2018**, 063207 (2018).
- [49] G. Nägele, A. J. Banchio, M. Kollmann, and R. Pesché, Dynamic properties, scaling and related freezing criteria of two- and three-dimensional colloidal dispersions, *Molecular Physics* **100**, 2921 (2002).
- [50] R. Pesché and G. Nägele, Stokesian dynamics study of quasi-two-dimensional suspensions confined between two parallel walls, *Phys. Rev. E* **62**, 5432 (2000).
- [51] A. Hashemi, R. P. Peláez, S. Natesh, B. Sprinkle, O. Maxian, Z. Gan, and A. Donev, Computing hydrodynamic interactions in confined doubly periodic geometries in linear time, *The Journal of Chemical Physics* **158**, 154101 (2023).
- [52] N. Liron and S. Mochon, Stokes flow for a Stokeslet between two parallel flat plates, *J. Eng. Math.* **10**, 287 (1976).
- [53] C. Manzo and M. F. Garcia-Parajo, A review of progress in single particle tracking: from methods to biophysical insights, *Reports on progress in physics* **78**, 124601 (2015).
- [54] M. Deforet, M. C. Parrini, L. Petitjean, M. Biondini, A. Buguin, J. Camonis, and P. Silberzan, Automated velocity mapping of migrating cell populations (avemap), *Nature methods* **9**, 1081 (2012).
- [55] P. A. Hassan, S. Rana, and G. Verma, Making sense of Brownian motion: Colloid characterization by dynamic light scattering, *Langmuir* **31**, 3 (2015).
- [56] K. A. Rose, M. Molaei, M. J. Boyle, D. Lee, J. C. Crocker, and R. J. Composto, Particle tracking of nanoparticles in soft matter, *Journal of Applied Physics* **127** (2020).
- [57] H.-P. Zhang, A. Be'er, E.-L. Florin, and H. L. Swinney, Collective motion and density fluctuations in bacterial colonies, *Proceedings of the National Academy of Sciences* **107**, 13626 (2010).
- [58] F. Peruani, J. Starruß, V. Jakovljevic, L. Søgaard-Andersen, A. Deutsch, and M. Bär, Collective motion and nonequilibrium cluster formation in colonies of gliding bacteria, *Phys. Rev. Lett.* **108**, 098102 (2012).
- [59] Z. Liu, W. Zeng, X. Ma, and X. Cheng, Density fluctuations and energy spectra of 3d bacterial suspensions, *Soft Matter* **17**, 10806 (2021).
- [60] Y. Fily and M. C. Marchetti, Athermal phase separation of self-propelled particles with no alignment, *Phys. Rev. Lett.* **108**, 235702 (2012).
- [61] F. Alarcón, C. Valeriani, and I. Pagonabarraga, Morphology of clusters of attractive dry and wet self-propelled spherical particle suspensions, *Soft matter* **13**, 814 (2017).
- [62] H. Chaté, F. Ginelli, G. Grégoire, and F. Raynaud, Collective motion of self-propelled particles interacting without cohesion, *Physical Review E* **77**, 046113 (2008).
- [63] F. Fadda, D. A. Matoz-Fernandez, R. van Roij, and S. Jabbari-Farouji, The interplay between chemophoretic interactions and crowding in active colloids, *Soft Matter* **19**, 2297 (2023).
- [64] V. Narayan, S. Ramaswamy, and N. Menon, Long-lived giant number fluctuations in a swarming granular nematic, *Science* **317**, 105 (2007).
- [65] J. Toner, Y. Tu, and S. Ramaswamy, Hydrodynamics and phases of flocks, *Annals of Physics* **318**, 170 (2005).
- [66] A. L. Thorneywork, S. K. Schnyder, D. G. A. L. Aarts, J. Horbach, R. Roth, and R. P. A. Dullens, Structure factors in a two-dimensional binary colloidal hard sphere system, *Molecular Physics* **116**, 3245 (2018).